Acta Biomaterialia xxx (xxxx) xxx

Contents lists available at ScienceDirect

Acta Biomaterialia

journal homepage: www.elsevier.com/locate/actbio

Full length article

Enamel-like stiffness achieved by poorly oriented nanocrystals in the capping tissue of Mexican beaded lizard osteoderms

Adrian Rodriguez-Palomo [a], Malene Siri Berg Jacobsen [a], Thorbjørn Erik Køppen Christensen [b,c], Mads Ry Vogel Jørgensen [a,b], Innokenty Kantor [b,d], Gabriella Willan [e], Anthony Herrel [f], Arsalan Marghoub [g], Mehran Moazen [g], Susan Evans [h], Matthew Vickaryous [e], Catherine J.A. Williams [i,*], Henrik Birkedal [a,*]

[a] Department of Chemistry and Interdisciplinary Nanoscience Centre (iNano), Aarhus University, 8000 Aarhus C, Denmark
[b] MAX IV Laboratory, Lund University, 224 84 Lund, Sweden
[c] DTU Compute, Danish Technological University, 2800 Kongens Lyngby, Denmark
[d] DTU Physics, Danish Technological University, 2800 Kongens Lyngby, Denmark
[e] Department of Biomedical Sciences, University of Guelph, Ontario N1G 2W1, Canada
[f] French National Centre for Scientific Research (CNRS) and National Museum of Natural History, 75005 Paris, France
[g] Department of Mechanical Engineering, University College London, Torrington Place, London WC1E 7JE, UK
[h] Department of Cell & Developmental Biology, University College London, Torrington Place, London WC1E 7JE, UK
[i] Department of Animal and Veterinary Sciences, Aarhus University, 8000 Aarhus C, Denmark

ARTICLE INFO

Keywords:
Heloderma horridum
Biomineral
X-ray diffraction
X-ray imaging
Nanostructure

ABSTRACT

Osteoderms, skeletal structures in the skin, are found in many animals and serve diverse roles. In some lizards, the bony osteoderm has a capping tissue (*CT*) whose composition and structure remain unknown. Here, the composition and nanostructure of osteoderms from the Mexican beaded lizard (*Heloderma horridum*) are investigated. The *CT* is highly mineralized with an extraordinarily high elastic modulus. Within the osteoderm, a transition zone between capping and bone tissue forms a graded increase in mineralization towards the superficial *CT*. Unlike other examples of mineralized tissues, the *CT* demonstrates a new combination of physical properties and nanostructural organization. It displays stiffness and hardness similar to enamel, and hydroxyapatite crystals that are an order of magnitude larger than those within the bone tissue and are, thus, reminiscent of enamel crystals. However, in stark contrast to enamel, the *CT* displays only minimal preferred orientation of the crystallites. Thus, it achieves very high mechanical properties with enamel-like crystal sizes but with near-isotropic microstructural orientation. The Mexican beaded lizard *CT* presents a highly unusual structural design resulting in high-performance mechanics.

Statement of Significance: The stiffest tissue in vertebrates is enamel, which is characterized by large, highly oriented nanocrystals. The less stiff bone has smaller nanocrystals and a lower, but still high degree of texture. The osteoderms of the Mexican beaded lizard are herein investigated by a combination of mechanical testing, spatially resolved X-ray diffraction and fluorescence, and 3D X-ray imaging. Surprisingly, the osteoderms have a capping tissue with enamel-like stiffness, significantly larger crystals than the underlying bone but are much less textured. This provides a new type of design for hard biological tissues.

1. Introduction

The skin of many living vertebrates is reinforced by elements such as scales, scutes, and osteoderms, among others, some of which are biomineralized and form tessellations. These structures have varied compositions and roles and are of profound interest to biomimicry [1–4]. Examples of mineralized tissues within the skin include the scales of fish and osteoderms in extinct and extant terrestrial vertebrates, including some dinosaurs [5] mammals [6], and reptiles including crocodilians, chelonians, lizards [7] and, rarely, snakes [8]. These osteoderms represent manifestations of the dermal skeleton, which first appeared in jawless fish approximately 500 million years ago and has been reduced

* Corresponding authors.
E-mail addresses: catherine.williams@anivet.au.dk (C.J.A. Williams), hbirkedal@chem.au.dk (H. Birkedal).

https://doi.org/10.1016/j.actbio.2025.08.025
Received 16 December 2024; Received in revised form 29 July 2025; Accepted 12 August 2025
Available online 14 August 2025
1742-7061/© 2025 The Authors. Published by Elsevier Inc. on behalf of Acta Materialia Inc. This is an open access article under the CC BY license (http://creativecommons.org/licenses/by/4.0/).

Please cite this article as: Adrian Rodriguez-Palomo et al., *Acta Biomaterialia,* https://doi.org/10.1016/j.actbio.2025.08.025

and elaborated across vertebrate taxa since [9]. This dermal skeleton is very diverse, heterogeneously expressed, and present in some members of most vertebrate lineages, with a wide range of hypothesized functions ranging from defense against predators [10–12] or conspecifics [13], thermal [14] or mineral storage [15], to contribution to biomechanics [16,17].

In tetrapods, the widest variation of skin mineralization is seen in the osteoderms of lizards. These skeletal elements are located within the dermis and complement the axial and appendicular skeleton used for support and muscle attachment [9]. The diversity of lizard osteoderms includes not only their presence or absence in a given species but also the extent of their body coverage, histological appearance, and structural characteristics [7].

Recently, it has become apparent that osteoderms in some species present a superficial, highly mineralized layer, called capping tissue (*CT*) [7,18,19]. Previous work in *Heloderma suspectum*, a sister species to that presented in this work, showed high stiffness in the *CT*, with mean values of 27.1 GPa using nanoindentation [19] and 21 GPa using atomic force microscopy [18], which contribute to low tissue level strain, and reach values close to the lizard's tooth enamel. The CT also displays different histological staining properties from the bone of the osteoderm and is associated with low intrinsic collagen and low cellularity [17,19]. In other apatite-based biological systems, high stiffness and low collagen content are observed in ganoine in fish scales [20–22], tooth enamel [23,24], and the enamel-like apatite crown of crayfish mandibles that cover a composite of chitin and amorphous mineral [25]. Common to these systems is a high degree of preferred orientation of the apatite crystals, resulting in anisotropic mechanical properties parallel to the *c*-axis of the apatite crystals [26,27].

The different material and histological properties from those of bone make the *CT* of high interest for material scientists interested in biomimicry, but also to evolutionary and developmental biologists focused on the diversity of biomineralization and the potential connection of this tissue type to the proposed ecological functions of osteoderms. The current knowledge of the chemical makeup and crystalline structure of these capping layers is restricted to single fossils and living species [5,18].

In particular, the osteoderms of *Heloderma* spp., exhibit a thick layer of *CT*, which presents an intriguing and quantifiable link to function, given reports of female-female and male-male aggression within the species, and the presence of bite force measurements that can be compared with the material properties of the osteoderms [28]. Therefore, we investigate samples from this taxon to shed light on the biomineral phase using e.g. nanoindentation, X-ray tomography, and scanning X-ray diffraction (XRD) and X-ray fluorescence spectroscopy (XRF).

2. Materials and methods

2.1. Sample preparation

Osteoderms orignated from two lizard specimens in the collection of Anthony Herrel and MNHM (National Museum of Natural History), made available for previous study [17]. The *Heloderma horridum* species is protected under the Convention on International Trade in Endangered Species of Wild Fauna and Flora (CITES), Appendix II. The access to such species is naturally limited, and therefore, only two individuals were included in this study. The osteoderms were fixed tissue specimens of epidermis and dermis containing osteoderms from the dorsal cervical midline of adult female *Heloderma horridum* (Individuals 1 and 2, collection ID Herrel: heh2, MNHM 1201) of snout-vent length 317 mm and 271 mm, respectively. The fixation process was performed by placing the tissue in 10 % aqueous formaldehyde for 48 h, after which it was rinsed and transferred to 70 % ethanol for storage. Skin samples and isolated osteoderms were photographed and studied using 3D X-ray microscopy. The six osteoderms from Individual 1 and one osteoderm from Individual 2 were used in the employed techniques as indicated in Table 1. For scanning X-ray diffraction (XRD) and X-ray fluorescence (XRF), two adjacent osteoderms (osteoderms #1 and #2, from Individual 1) were embedded in EpoFix resin (Struers ApS, Denmark) with a curing time of 24 h, after which they were demolded and sequentially sliced in the transverse and sagittal planes, respectively, using a diamond-blade saw (Accutom-5, M1D15 wheel, Struers, Ballerup, DK). The obtained slices (~280 μm thick) were then placed on Kapton tape and mounted on metallic frames for the XRF/XRD experiments.

A third osteoderm from the skin sample from Individual 1 was isolated with all the surrounding soft tissue (osteoderm #3), suspended in ethanol-infused agar gel, and its 3D structure was investigated by 3D X-ray microscopy. Additional osteoderms were embedded in resin and sliced for the study of local mechanical properties (osteoderms #4 and #7 from individuals 1 and 2, respectively), fracture surface morphology by electron microscopy (osteoderms #4 and #5), and histology (osteoderm #6).

2.2. 3D X-ray microscopy and computed tomography

The osteoderm morphology was studied by X-ray microtomography in a Versa 620 X-ray microscope (ZEISS, Germany). X-rays were produced with an accelerating voltage of 40 kVp and a power of 3 W and filtered using a low-energy filter. A total of 3201 X-ray projections in the range 0 – 360° with an exposure time of 12 s were collected on a CCD camera coupled to a 4× magnification objective equipped with a scintillator. The tomographic reconstructions were conducted using the TXM Reconstructor Scout-and-Scan software provided with the instrument (ZEISS, Germany) using a cone beam adapted filtered back projection (FBP) algorithm, resulting in an isotropic voxel size of 1.498 μm. The tomographic slices were processed and analyzed using the software Dragonfly (Comet Technologies Canada Inc.). The 3D volumes containing bone (*BT*), capping tissue (*CT*), and the voids in the osteoderm were segmented by thresholding. The transition zone (*TZ*) was defined by applying dilation operations to the *BT* and *CT* segmented volumes. Once defined, the segmented volume for the *TZ* was subtracted from the *BT* and *CT* volumes.

Additionally, low-resolution scans were made before slicing for scanning XRD experiments. An accelerating voltage of 70 kVp and a power of 8.5 W were used in combination with a low-energy filter. An exposure time of 2 s per projection was used, measuring a total of 1601 projections in the range 0 – 360°. The detector was placed behind a 0.4× objective equipped with a scintillator and a 2 × 2 detector pixel binning was employed, resulting in a voxel size after a FBP reconstruction of 40.570 μm.

X-ray transmission radiographies were measured on the slices used for scanning XRD and XRF (~280 μm thick). The X-ray transmission images were obtained by averaging 10 radiographies collected with a 5 s exposure time each. Flat field correction was applied to the images using 10 images and 5 s exposure time for each. A 2 × 2 detector pixel binning was applied to improve the signal-to-noise ratio, obtaining a pixel size of 5.004 μm.

2.3. Synchrotron tomography

Synchrotron tomography was collected at the DanMAX beamline of the MAX-IV laboratory synchrotron (Lund, Sweden). A 25 keV X-ray beam was obtained using a Si(111) double-crystal monochromator, obtaining a beam size of 1.13 × 1.18 mm^2 ($H \times V$). The skin sample containing the osteoderm was embedded in Ethanol-infused agar gel (70 % Et-OH) and placed in a motorized rotatory stage. An sCMOS camera (Orca lightning) and a 10× objective with a 100 μm LuAG:Ce scintillator (Crytur) at 45 mm from the sample were used to collect 6400 projections of 2592×4608 pixels each with a rotation step of 0.056 degrees between 0 – 360° using an exposure time of 15 ms per projection. 50 dark and flat field images were collected during the measurement to correct the

Table 1
Summary of experiments conducted and samples used in each.

Individual	Osteoderm #	3D X-ray microscopy	Synchrotron tomography	Scanning XRD/XRF	Nanoindentation	SEM	Histology
1	1	X		X			
1	2	X		X			
1	3	X	X				
1	4				X	X	
1	5					X	
1	6						X
2	7				X		

measured projections. 4 of such datasets were then stitched together to form a set of 6400 projections with 6391×2142 pixels or approximately 3.515×1.18 mm^2 ($H \times V$) field of view and an isotropic voxel size of 550 nm. A computed tomography reconstruction was done using the DanMAX in-house software based on the Tomopy package [29].

2.4. Scanning X-ray diffraction and fluorescence

Combined scanning X-ray diffraction (XRD) and X-ray fluorescence (XRF) were performed at the DanMAX beamline of the MAX IV laboratory synchrotron (Lund, Sweden). A 17 keV X-ray beam was obtained using a Si(111) double-crystal monochromator and focused using a compound refractive lens transfocator to a beam size (full-width half maximum) of 43.9 × 15.0 μm^2 (horizontal × vertical). A motorized stage with 2-axes movement in the plane perpendicular to the beam was used to raster scan the osteoderm slices with fly-scanning movement in the vertical direction. For high-quality signal to noise, a scanning rate of 80 Hz (exposure time of 12.5 ms per point) was used in steps of 20×10 μm in the horizontal and vertical directions, respectively. The X-ray diffraction signal was recorded in transmission geometry using a PILATUS3×2M CdTe detector [30] (Dectris, Switzerland) at a sample-to-detector distance of 0.23498 m. A tungsten beam stop between the sample and the detector was used to block the direct beam. The beam stop had an internal Al wire, stopping the fluorescence from the tungsten L edge. The fluorescence signal from the sample was measured using a SiriusSD detector (RaySpec Ltd., UK) at a distance of 175 mm and an angle of 36° relative to the incident beam. Two perpendicular osteoderm slices (transverse and sagittal) were measured to account for any possible texture artifacts.

The measured diffraction signal was radially integrated with the software MatFRAIA [31], obtaining a q-range of 1.5 – 41.6 nm^{-1}. The integrated diffraction data were Rietveld refined using a hydroxyapatite model with the software MultiRef [32] and GSAS [33] using data in the range q = 16.64 – 39.96 nm^{-1}. The model used consisted of a background function (10 coefficient Chebyshev polynomial expansion), lattice constants, scale factor, profile parameters describing the anisotropic size broadening as well as a spherical harmonics description of preferred orientation. The obtained refinement results were combined into the corresponding 2D images, excluding points where convergence was not achieved (these were points without any diffraction signal). A final intensity mask was applied to remove the area outside the osteoderm. The XRF data was processed and fitted using the software PyMCA [34] to map variations in elemental composition across the osteoderm and masked in the same manner as the XRD results.

The crystal orientation analysis was also performed using the Angular Gaussian Fitter (AGUF) software package [31]. A q-range containing the (002) reflection (q = 1.80 – 1.85 nm^{-1}) was radially and azimuthally integrated using 360 azimuthal bins using the above-mentioned integration strategy. The orientation and degree of orientation were calculated using a series of Gaussian peaks fitted to the azimuthal intensity distribution after a local background in the azimuthal component, as previously described by Chua et al. [35]. The quality of the fits for representative points in *BT* and *CT* are shown in Supporting **Figures S13** and **S14**.

2.5. Nanoindentation

Nanoindentation measurements were performed on one *Heloderma horridum* osteoderm each from two different individuals (Osteoderms #4 and #7, Table 1), embedded in Epofix resin and sliced using a diamond saw as described above. The final surface preparation was accomplished by polishing with silicon carbide paper (800, 1200, 2400 grit) and a diamond suspension with a final roughness of ~1 μm. A Hysitron TriboIndenter (Hysitron, Minneapolis, MN) with a Berkovich tip was used to measure maps using a maximum load of 1000 μN and a distance between indents of 25 μm. A 10 s load, 30 s stabilization time and 10 s unload scheme were used to ensure relaxation of viscoelastic effects. The unloading segment in each indent was fitted and the reduced elastic modulus (*Er*) and hardness (*H*) were calculated using the Oliver-Pharr method [36]. The distance dependence of the obtained values relative to the *TZ* were fitted using a sigmoidal function with a linear component.

$$y(x) = A_2(1 + \alpha \cdot x) + \frac{A_1 - A_2}{1 + e^{-\frac{x - \mathrm{abs}(x_0)}{dx}}} \quad (1)$$

2.6. Scanning electron microscopy (SEM)

Scanning electron microscopy images from the capping tissue and bone tissue of two osteoderms were acquired using a TESCAN CLARA (S8151). The osteoderms, including the dermis, were fractured to expose the crystalline particle morphology, mounted on vertical aluminum stubs, and coated with 8 nm of platinum. An acceleration voltage of 15 keV and a current of 300 pA were used at a working distance of 5 mm.

2.7. Statistical analysis

The data presented belongs to two individuals of *Heloderma horridum:* Heh1 for Osteoderms #1–6 and Heh2 for Osteoderm #7. A total of 7 osteoderms were used for the experiment as described in Table 1. Data are presented as mean ± standard deviation unless specified otherwise. Statistics were performed in *R* Studio (R version 4.3.1) using packages tidyverse, lme4, lmtest, DHARMa, ggplot2, emmeans. For analyzing crystal parameters between defined regions from the XRD data on osteoderms #1 and #2, and for analyzing reduced Young's modulus and hardness in the nanoindentation data on osteoderms #4 and #7, general linear models were constructed with osteoderm and region as fixed effects, and a gamma log link of the form model_1 <- glm (Variable ~region_name + osteoderm + family = Gamma (link="log"), data = data). All pairwise comparisons are performed on the response variable of the predicted outcomes. Model features of normality and homoscedasticity were assessed visually as acceptable. The p-values of pairwise comparisons are adjusted for multiple comparisons using Tukey's method, and given the number of observations allowed by the resolution of the techniques employed, are provided for indication only. Descriptive statistics and results of pairwise comparisons, as highlighted in the text, are provided in the Supporting Information (Figures S9 and S10 and Table S1).

3. Results

Osteoderms in the Mexican beaded lizard (Fig. 1a,b) have an oblate morphology with distinct 'dimples' on the superficial dorsal (exterior) surface. Their gross morphology and relative placement in the skin, obtained by low-resolution X-ray microscopy, are shown in Fig. 1c,d, where the X-ray absorption values corresponding to the mineralized tissue, are segmented and 3D rendered. The osteoderm marked '1′ in Fig. 1c,d has an apparent area of damage or defect (arrow in Fig. 1c,d) of unknown origin. Higher resolution 3D X-ray microscopy of an extracted osteoderm reveals more structural information in Fig. 1e,f, and **Supporting Video S1**. The X-ray absorption, displayed as the grayscale value, is proportional to the material density, which here corresponds to the degree of mineralization. The osteoderm shape is consistent with previous observations in osteoderms from the sister taxon *Heloderma suspectum* [17–19,37]. Capping tissue (*CT*) is present across the superficial section of the osteoderm and has a higher X-ray absorption, reflecting its higher degree of mineralization compared with the bone tissue (*BT*) of the rest of the osteoderm. Note that the X-ray absorption contrast in the capping tissue is not homogeneous, being higher at the top of the knobs. A gradient in the absorption contrast between *CT* and *BT* is observed in a virtual slice (Fig. 1g–j), indicating a smooth decrease

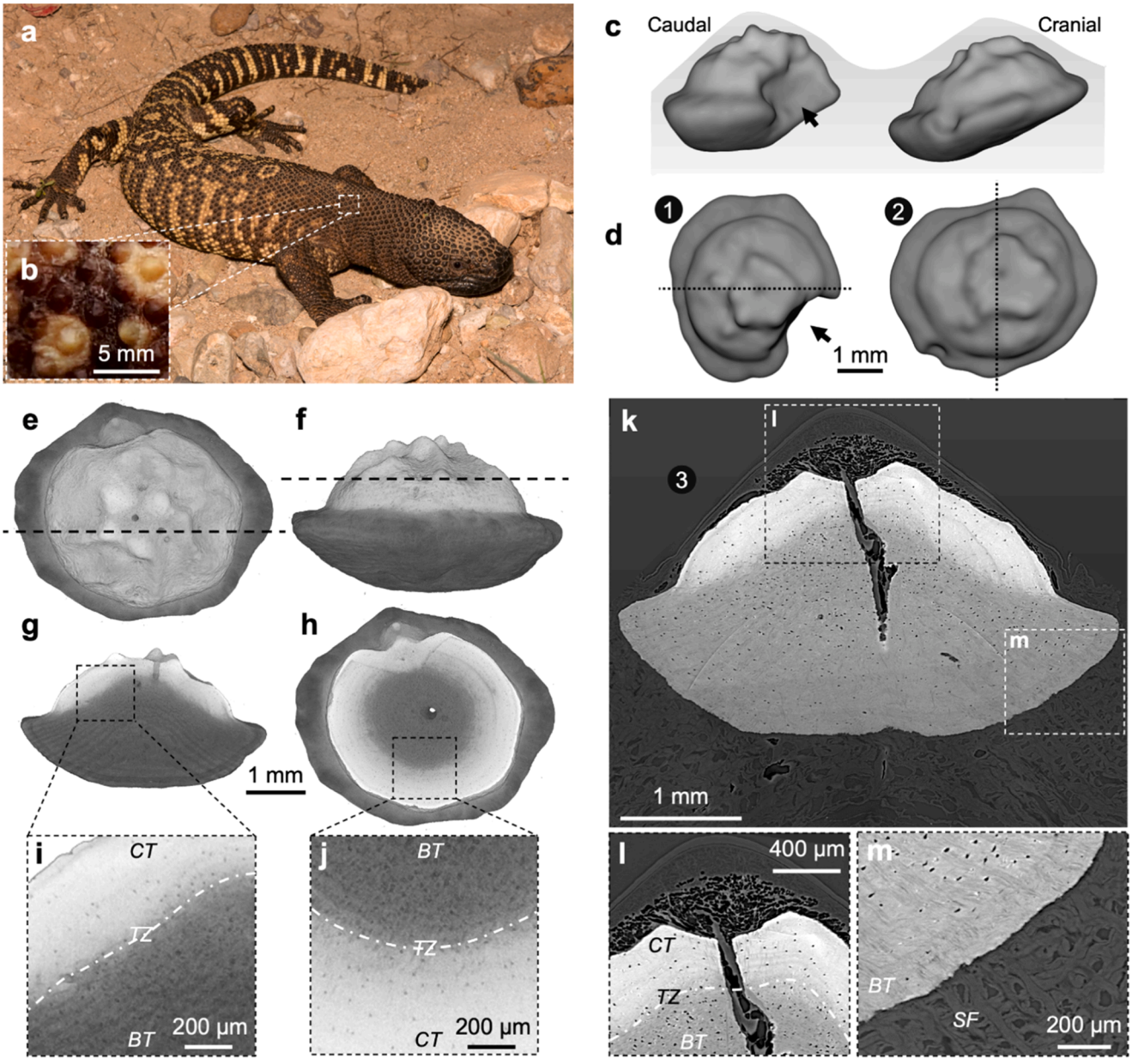

Fig. 1. a) *Heloderma horridum* (Mexican beaded lizard) (Credit: Andrew DuBois, CC BY-NC 2.0) and **(b)** detail of a skin sample used for the experiments. **c)** Lateral and **(d)** dorsal view of the two adjacent osteoderms measured in the scanning experiments using X-ray computed tomography. The 3D render of the segmented mineralized tissue of osteoderm #1 (left) and #2 (right) before slicing, i.e. in their original relative location. The dotted lines show the location and orientation of the extracted 2D slices, and the arrows show apparent damage in osteoderm #1. The light gray background in pane (c) demarks a sketch of the outline of the surrounding skin, which was added *a posteriori* to guide the eye. **e-j)** X-ray computed tomography 3D data (voxel size: 1.5 µm). Dorsal **(e)** and lateral **(f)** views of osteoderm #3. **g, h)** Virtual slice following the dashed lines in e and f. **i, j)** Higher magnification images of the virtual slices showing the mineral contrast in bone tissue (*BT*), capping tissue (*CT*), and their transition zone (*TZ*). **k-m)** Synchrotron X-ray computed tomography with phase contrast (voxel size: 550 nm) showing **(k)** a virtual slice of the osteoderm embedded in the surrounding soft tissue, and two higher magnification images highlighting **(l)** the porosity of *CT, BT*, and *TZ* as well as **(m)** the Sharpey fibers (*SF*) running into the BT.

in the degree of mineralization from CT to BT. Henceforth, we refer to this region of declining mineralization density as the transition zone (*TZ*). Large channels traversing the osteoderms vertically from ventral to dorsal can also be observed, as in Fig. 1k and 1l; they have previously been identified as neurovascular canals [7,37]. We also investigate the osteoderm by synchrotron phase contrast X-ray tomography, collected at the 4th generation synchrotron MAX IV (Lund, Sweden) at the DanMAX beamline, to reveal the interface between mineralized osteoderm and soft tissue. A layered structure with alternating high and low absorption contrast in the *BT* can be seen in Figs. 1k and 1m, corresponding to the insertion of Sharpey's fibers previously seen in histological studies [37]. The *CT* is found by histology to have very low, if any, collagen content in comparison with the underlying bone of the osteoderm, as shown in **Supporting Figure S11**.

The local mechanical properties of the different tissue types in the osteoderms from two separate individuals (osteoderms #4 & #7) were investigated by nanoindentation (Fig. 2). The mechanical properties of the *BT* agree with previously reported values in lizard *BT* [19,38]. Surprisingly, however, the elastic modulus and hardness of the *H. horridum CT* are higher than reported data in other lizard species [19] reaching up to 100 GPa at the most dorsally superficial part of the capping tissue. *H. horridum* thus presents the highest *CT* stiffness found across different lizard species thus far. The stiffness follows a sigmoidal increase at the *TZ* on top of a linear increase in the *CT* and *BT*. The fitted model (see model parameters in the Methods section, Tables 2 and 3) shows that the mechanical properties are not constant within the *BT, TZ*, and *CT*. Therefore, they cannot be averaged for the two different tissue

Table 2
Nanoindentation distance dependence fitting parameters ± standard deviation used in Eq. (1) for osteoderm #4. Values are given with at least 2-digit precision even when the standard deviation was higher.

Magnitude	A_1	A_2	x_0	α	dx
Elastic modulus	50.6 ± 7.8	8.54 ± 3.67	60.07 ± 0.59	0.035 ± 0.027	1.16 ± 0.53
Hardness	2.64 ± 0.48	0.16 ± 0.21	60.66 ± 0.72	0.072 ± 0.13	1.61 ± 0.66

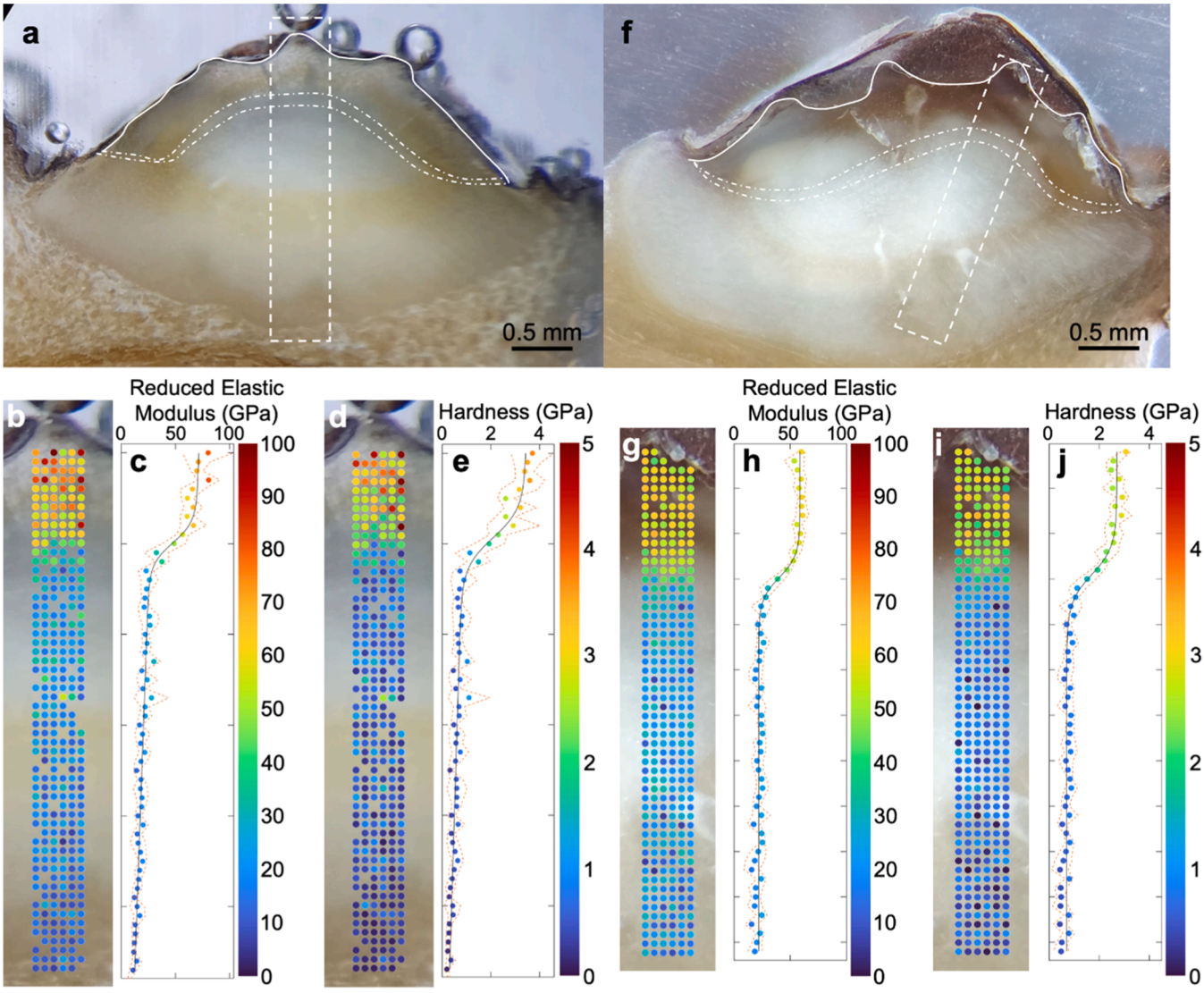

Fig. 2. Mechanical properties of capping tissue (*CT*) and bone tissue (*BT*) in two *Heloderma horridum* osteoderms #4 and #7 from different individuals obtained by nanoindentation mapping. **a, f)** Osteoderm overview with the mapped area highlighted by the dashed boxes. The osteoderms *CT* surface is highlighted with solid lines and the transition zone between *CT* and *BT* is highlighted with dot-dashed lines. **b, g)** Reduced elastic modulus (E_r) and **(d, i)** hardness (H) for each indent represented with a dot according to the color scale, and **c,e, h, j)** mean value and standard deviation as a function of distance. The dashed orange lines represent ± one standard deviation. The solid black curve shows the fit of a linear function with a sigmoidal function describing the transition from *BT* to *CT*.

Table 3
Nanoindentation distance dependence fitting parameters ± standard deviation used in Eq. (1) for osteoderm #7. Values are given with at least 2-digit precision even when the standard deviation was higher.

Magnitude	A_1	A_2	x_0	α	dx
Elastic modulus	58.7 ± 1.9	21.96 ± 0.95	14.83 ± 0.47	0.00 ± 0.00	1.21 ± 0.41
Hardness	2.71 ± 0.11	0.70 ± 0.050	14.51 ± 0.53	0.00 ± 0.00	1.53 ± 0.45

types of bone and capping and reflect a higher structural complexity than previously believed. The reduced elastic modulus (*Er*) and hardness (*H*) of *BT* present a mean elastic modulus between $Er = 11 \pm 4$ to $Er = 23 \pm 7$ GPa, and a mean hardness between $H = 0.18 \pm 0.07$ to $H = 0.7 \pm 0.3$ GPa (Values are reported as mean ± standard deviation where the standard deviation is a measure of the spatial variation across the region). In contrast, the *CT* is both biologically and statistically stiffer and harder **(Table S1)**, with a mean elastic modulus between $Er = 54 \pm 8$ and 81 ± 10 GPa and a mean hardness between $H = 2.5 \pm 0.4$ and 3.6 ± 0.6 GPa. The variation comes from the fact that different areas in the capping tissue, especially the most upper part of the knobs, show a different degree of mineralization, as shown in Fig. 1. The *TZ* shows a progressive change between the mechanical properties of *BT* and *CT*, with an increment of $\Delta Er = 56$ GPa and $\Delta H = 2.6$ GPa over a distance of ~1 mm. This region matches our previous observations of a graded interface between tissues (the *TZ*) in the X-ray absorption images in Fig. 1.

To shed light on the origin of these drastic spatial variations in mechanical properties, two slices in the longitudinal and transverse directions from adjacent osteoderms, as indicated in Fig. 1d, were investigated using synchrotron scanning XRD/XRF. The XRD and XRF signals in each of the 58,722 points were simultaneously collected by appropriate detectors (See **Supporting Figure S1**).

The maps in Fig. 3 show the element-specific fitted XRF signals for

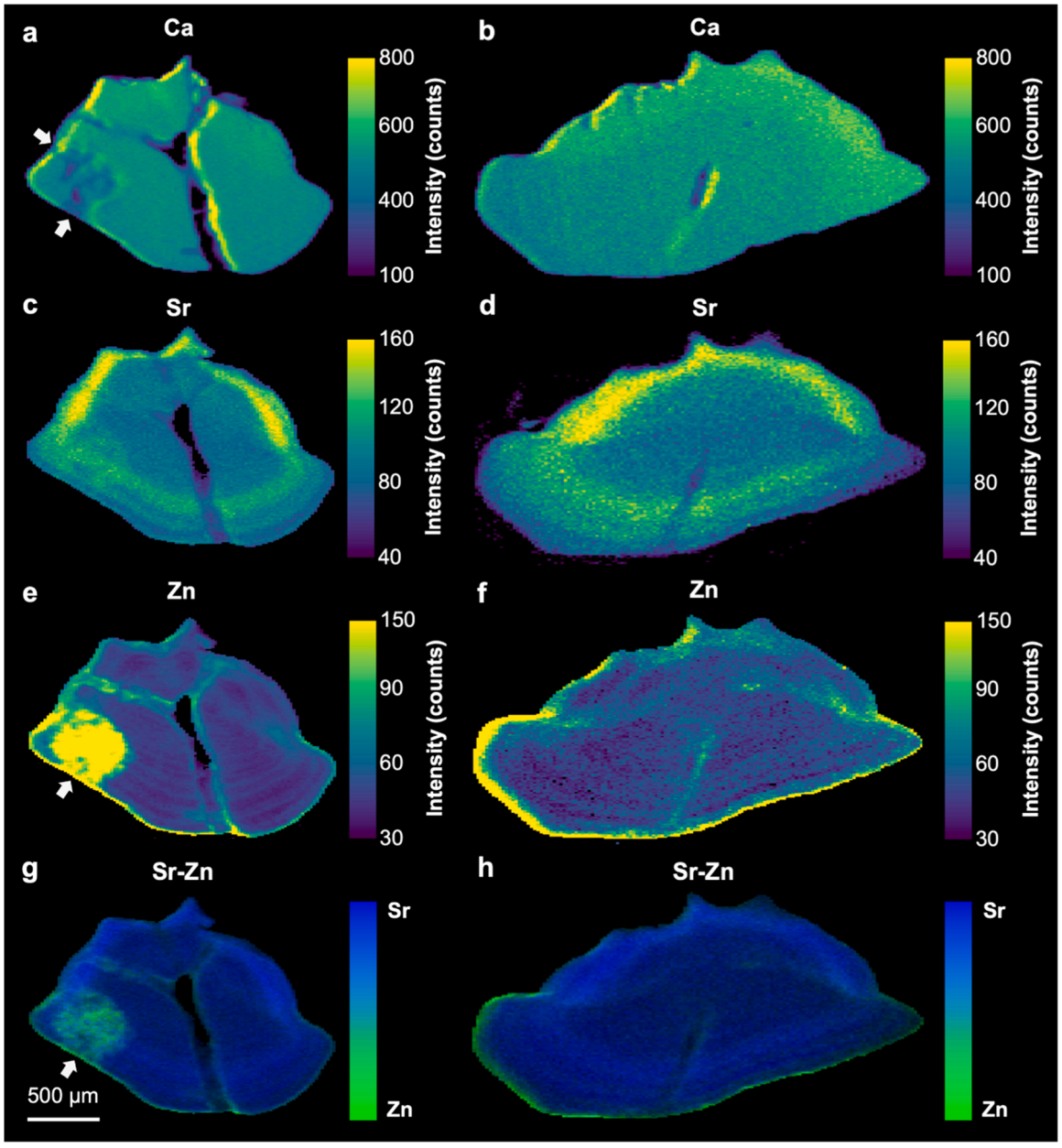

Fig. 3. Scanning X-ray fluorescence spectroscopy of a 2D slice in osteoderm #1 **(left)** and osteoderm #2 **(right)**. Elemental maps of **(a, b)** calcium (Ca), **(c, d)** strontium (Sr), **(e, f)** zinc (Zn), and **(g, h)** overlapped intensity maps of normalized Sr and Zn intensities. Arrows point to sites of abnormal element content.

the two slices through the osteoderms. Additionally, the *BT, CT*, and their *TZ* were manually segmented, and their histograms were calculated with normalization for the number of data points, as shown in **Supporting Figure S2**.

The calcium maps in Fig. 3a,b show no significant features or contrast and are highly homogeneous across the entire osteoderm with the obvious exception of the neurovascular canal. This lack of variation results from sample self-absorption, which results in only slightly higher calcium content being observed in the *CT* (see also the histograms of segmented maps in **Supporting Figure S2e,f**). The escape depth (i.e., the distance where self-absorption reduces the emitted X-ray photon flux to 1/e) of the emitted fluorescence photons in *BT* containing a mineral fraction of 50 % hydroxyapatite is ~23.5 μm for the Ca *K* emission at 3.69 keV [39]. In contrast, the corresponding escape depth for the heavier Sr *K*-edge is ~308 μm. Hence, the Ca *K*-maps only report on the outermost surface of the sample, while, for example, Sr *K*-maps represent bulk Sr-concentration. The escape depth means that Ca lights up on the left edge, as that side is the direction of the detector, as for the pixels closest to the edge, the full thickness can be seen in the Ca signal. In addition to Ca-fluorescence, we observed significant Sr and Zn *K*-edge fluorescence (**Figure S2a**). These important oligo-elements were found to be localized in specific areas, Fig. 3c,d, and Fig. 3e,f. Strontium is mainly present in the *CT* (see Fig. 3c,d, and histograms in **Supporting Figure S2g,h**). In contrast, zinc is localized to the external border of the osteoderm and *TZ* (Fig. 3e,f). Furthermore, concentric bands with high strontium and zinc content are visible in the *BT*. Almost no spatial overlap is observed between strontium and zinc, as shown in the combined element maps in Fig. 3g,h. Additionally, high zinc and low

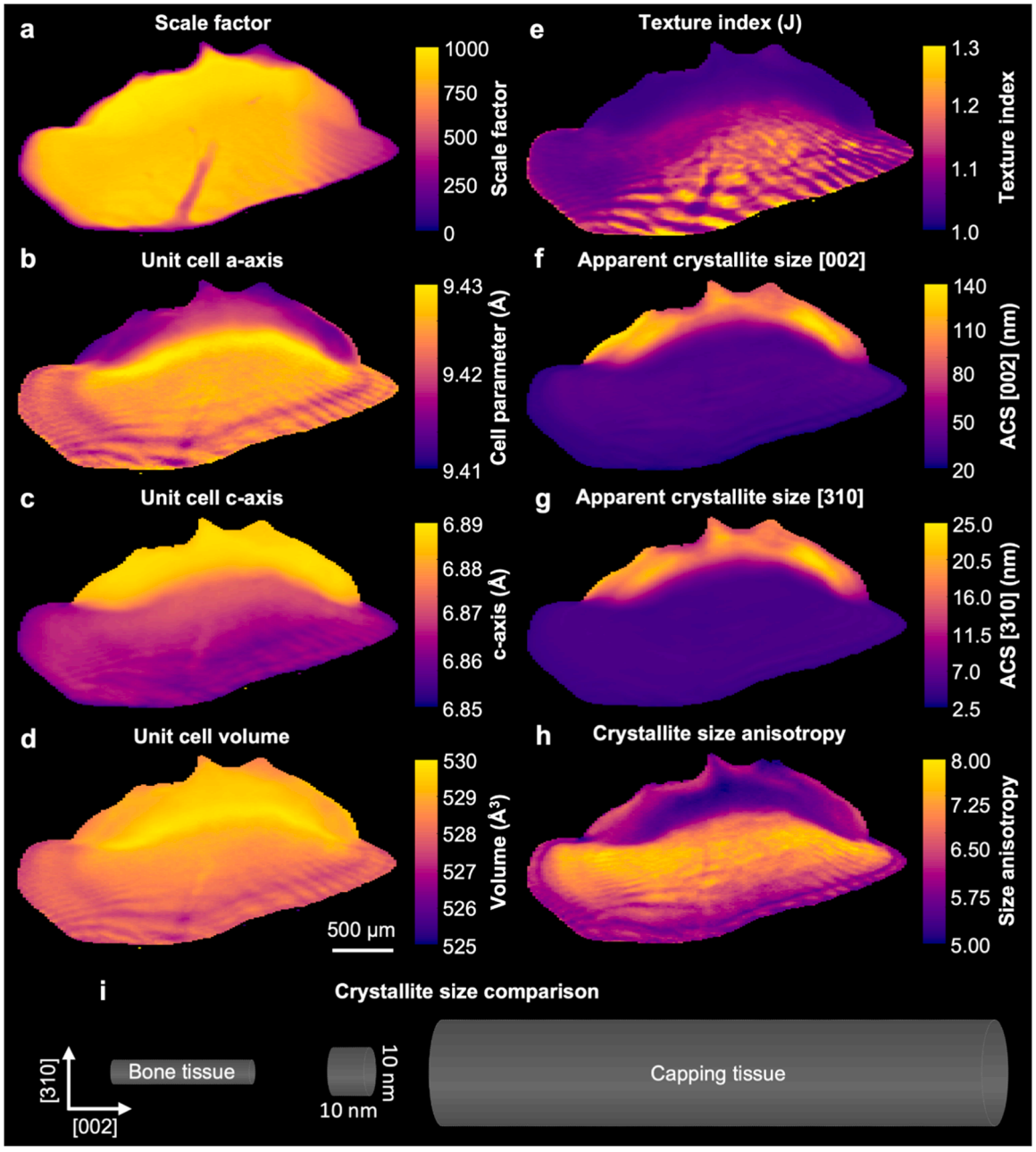

Fig. 4. Scanning X-ray diffraction of osteoderm #2. **a-e)** Rietveld refined crystallographic parameters for a hydroxyapatite model: **(a)** scale factor, **(b)** unit cell a-axis, **(c)** unit cell c-axis, **(d)** unit cell volume, and **(e)** texture index. **f-h)** Apparent crystallite dimensions calculated from the refined peak positions and full-width at half maximum (FWHM) (See **Supporting Figure S5**): **(f)** apparent crystallite size perpendicular to the [002] and **(g)** [310] crystallographic direction, **(h)** estimated crystallite shape anisotropy, and **i)** representation of the crystallite seizes for *BT* and *CT*. See **Supporting Figure S3** for equivalent information on osteoderm #1.

calcium intensities are visible in part of the *BT* in osteoderm #1 (see arrows in Fig. 3a,e). This region corresponds to the area of apparent damage seen in the X-ray CT scans in Fig. 1c,d. The low calcium content indicates a reduced degree of mineralization in the region, reflecting the damage. A very localized and anomalously high zinc content suggests an ongoing remineralization phase. Indeed, zinc has been reported to be up-concentrated in growth areas, indicating sites of ongoing mineralization. It has been located in the extracellular matrix before and at the mineralization front [40] as well as during the fracture healing process [41], possibly as a cofactor of multiple metalloproteases [42,43]. We, therefore, suggest that the osteoderms undergo repair upon damage in a process reminiscent of fracture healing or general bone remodeling. Iron was previously found coating the tooth enamel in various species of reptiles [44]. No localized iron was found in the osteoderm *CT* or *BT*.

The scanning XRD data were collected concurrently with the scanning XRF data and were analyzed by Rietveld refinement of each point (see Methods) [32]. The investigated slices (Fig. 1d) sampled two perpendicular cuts through the osteoderm to evaluate whether orientation effects may play a role. In the following section, we present results for osteoderm #2. Equivalent results for osteoderm #1 are found in the supporting information; all trends are similar in the two cross-sections, and no significant slice orientation effects are observed. The only mineral found in the osteoderm was hydroxyapatite-like, the biomineral phase of bone [45] (**Supporting** Fig. 1b). The diffractograms in *BT* display significant size broadening of the diffraction peaks, as expected for bone [46,47]. Surprisingly, diffractograms from the *CT* feature much sharper diffraction peaks indicative of large crystallites. The results of the Rietveld refinements are summarized in Fig. 4 and **Supporting Figure S3**. They confirm that the crystallites in the *CT* differ drastically from those in the *BT*, which is also confirmed by histograms of the Rietveld parameters for the different segmented areas (*BT, CT, TZ*) shown in Fig. 5 and **Supporting Figure S4**.

The Rietveld scale factor (Fig. 4a) is proportional to the number of diffracting unit cells, i.e., the volume fraction of crystalline material. It is higher in the *CT* than in the *BT* (Fig. 5c), reflecting the higher degree of mineralization in the *CT*. This agrees with the higher absorption values in the X-ray microscopy experiments (Fig. 1g) and the previously reported results in other lizard species [5,7,18]. It shows that the higher degree of mineralization observed in the X-ray computed tomography is due to an increased volume fraction of crystalline biomineral, rather than amorphous biomineral.

The unit cell *a*- and *c*-axes differ strongly between *BT* and *CT*. The unit cell *a*-axis in the *CT* is considerably smaller than in the *BT* (Fig. 4b**, Supporting Figure 9, Supporting Table S1**). Of all parameters considered, the unit cell *a*-axis is the only one where the value in the *TZ* falls outside the range between the values for the *BT* and the *CT*.

The *c*-axis in the crystalline lattice is significantly larger in the *CT* than *BT* (Fig. 4c**, Supporting Figure 9, and Supporting Table S1***)*. This results in a slightly larger unit cell volume (Fig. 4d**, Supporting table S1),** suggesting that the differences are not due to e.g., Sr-substitution alone [48]. Interestingly, the segmented histograms show a bimodal distribution for the lattice parameters, see Fig. 5d–f. The source of the two modes is the layered structure with high/low values, seen especially in the *BT*. A smooth *TZ* can be observed between the *CT* and the *BT*, as previously observed in the X-ray microscopy experiments, nanoindentation, and X-ray fluorescence (Figs. 1–3). The *TZ* has the highest unit cell volume due to an expanded *a*-axis, suggesting that the *TZ* displays a distinct crystallization pattern compared to either *CT* or *BT*.

We report the apparent crystallite size from the (002) and (310) diffraction peaks as obtained using Scherrer's equation and the refined peak position and full-width-half-maximum (FWHM), shown in **Supporting Figure S5**. The apparent crystallite size is a lower bound on the crystallite size in each pixel since effects of disorder and/or strain may contribute. The apparent crystallite size in the [002] direction reflects the length of the crystals. It is below 40 nm in the *BT,* following results reported in the literature [49], but is drastically enlarged to values that can exceed 100 nm in *CT* (Fig. 4f, Fig. 5h**, Figure S9, Table S1**). The apparent crystallite size from the (310) diffraction peak, related to the crystallite width, presents values of up to 5 nm in the *BT*, again in agreement with literature for general bone, but is drastically increased to reach 25 nm in the *CT* (Figs. 4g and 5i**, Figure S9, Table S1**). The biomineral hydroxyapatite crystals in the osteoderm are, therefore, elongated needle- or platelet-like, with nearly an order-of-magnitude larger crystals in *CT* than in *BT*. The hexagonal bio-apatite crystals are thus anisotropic in shape. A measure of the crystallite size anisotropy can be obtained as the ratio of the size parallel and perpendicular to the *c*-axis. This apparent crystallite shape anisotropy in Fig. 4h shows that the biomineral crystals are more anisotropic (i.e., more elongated) in the *BT* with a rim of smaller values towards the osteoderm upper surface, compared to those in *CT*, which decreases radially to more isotropic shapes. The *CT* presents large crystals with a lower length/width ratio than in *BT*.

The Rietveld refinement also produces a measure of the degree of texturing (Figs. 4e and 5g) through the texture index [33]. The values in *BT* display a spatially varying pattern with values of the texture reaching 1.3, with a texture index of 1 corresponding to a fully randomly oriented powder. Given the larger needle-shaped crystals in the *CT* and by analogy with the highly textured enamel [23,50,51] one might expect the *CT* to be prone to microstructural arrangements, resulting in highly texturized XRD patterns. Surprisingly, the refined texture index presents a very low degree of texture in the *CT* (texture index ≈ 1.03). This can be observed visually as powder-like diffraction patterns (**Supporting Figures S13d,e**, and **S14d,e**). These findings suggest a microstructure with elongated hydroxyapatite crystals, a very isotropic microstructure, and orientation in the *CT*, resulting in powder-like diffraction patterns. Further insights into texture effects are obtained by analysis of the dependence of the intensity of the apatite (002) reflection on the azimuthal angle. This analysis shows low azimuthal dependency in the *CT* compared to the *BT*, as shown by the degree of orientation in **Supporting Figure S6a,b,** and in the histograms by the bimodal distribution between *CT* and *BT* (**Supporting Figure S7c,d** and **S8c,d**). While the degree of orientation is found to be low, there is also some consistency in the orientation, both in the *CT* and in the *BT*. In the *BT*, crystallites follow the orientation of the Sr bands (**Supporting Figure S6i,j**), whereas the hydroxyapatite crystallites in the *CT* always point towards the surface of the osteoderm (**Supporting Figure S6i,j**). While the degree of orientation is much smaller in the *CT* here, this orientation is reminiscent of that of the hydroxyapatite in the impact region of the stomatopod dactyl club [35,52].

The unexpectedly low degree of texture is further confirmed by electron microscopy. The crystallite particles were observed on fractured surfaces (**Supporting Figure S12**), where *BT* presents oriented mineralized collagen typical of bone, while *CT* has rounded isotropic particles with no apparent preferred orientation.

4. Discussion

Our results show that the Mexican beaded lizard (*Heloderma horridum*) osteoderms present a capping tissue (*CT*) with very high stiffness and hardness, which is comprised of large crystals with a surprisingly low degree of texture. This is established by a combination of techniques traversing length scales from the nano- to 100 μm scale and, in particular, reinforced by the ability at 4th generation synchrotrons to conduct large area scanning XRD/XRF, in the present encompassing ~30,500, which enables detailed correlative analysis over the specimen.

The species *Heloderma horridum*, native to the Pacific region of Mexico and Guatemala, is listed under the CITES agreement, Appendix II, which limits its availability to protect the species against trading. This limited the number of individuals in the study, which we attempted to compensate for by using imaging approaches, including both for structure and mechanics, that provided information on the entire osteoderm and using more than one specimen per individual whenever possible to

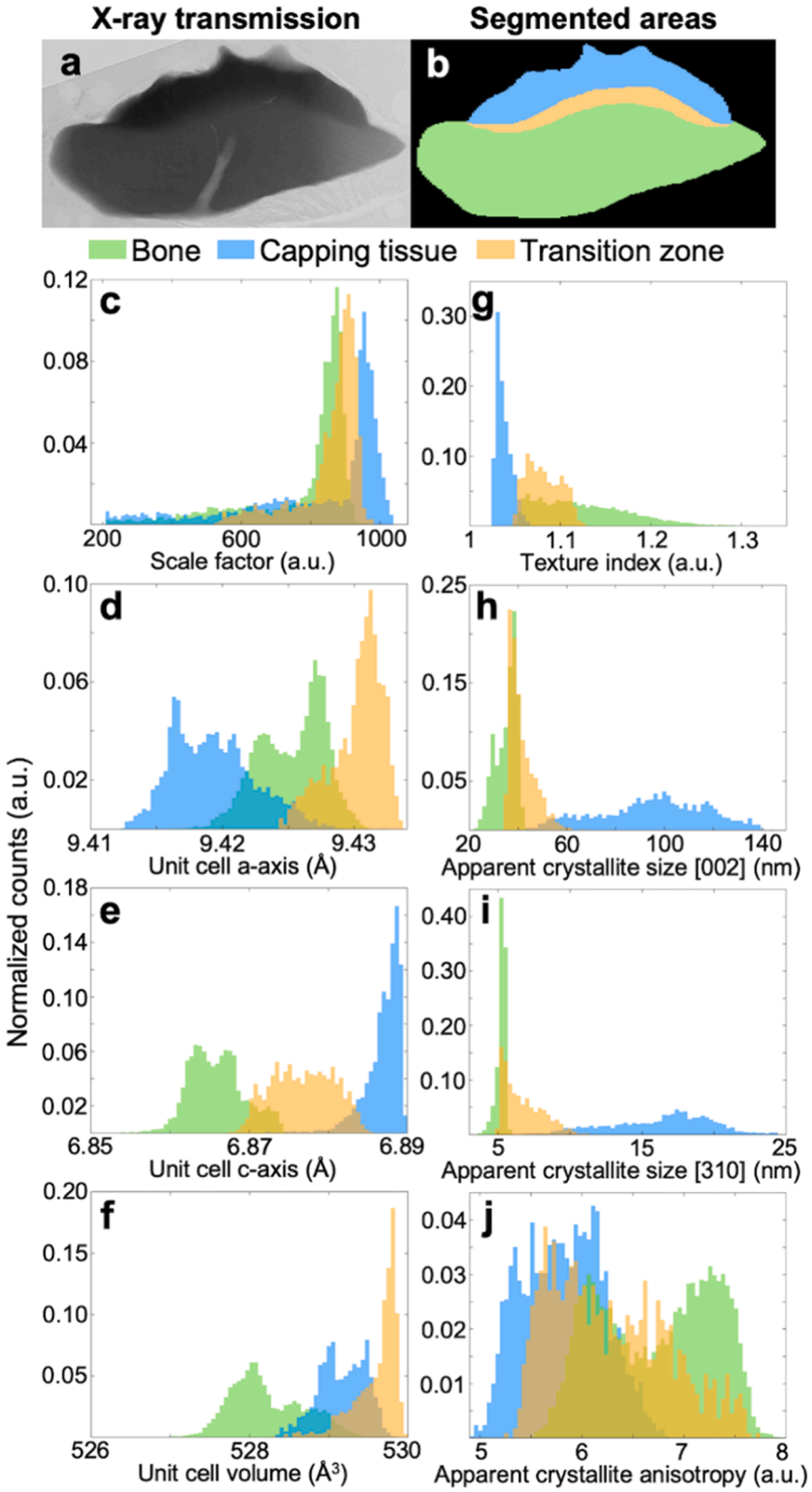

Fig. 5. Segmented areas and XRD histograms for osteoderm #2. **a)** X-ray radiography of the scanned 2D slices (pixel size: 5.00 μm). **b)** Segmented areas: bone tissue, capping tissue, and their transition zone. **c-j)** Histograms of the Rietveld refined crystallographic parameters and apparent crystallite dimensions in the segmented areas. See **Supporting Figure S4** for equivalent results from osteoderm #1.

account for possible variation between specimens.

4.1. Osteoderm morphology and microstructure: signs of remodeling

The osteoderms sampled are composed of bone tissue (*BT*) and *CT*, separated by a graded transition zone (*TZ*), except for the unit cell *a*-axis, which transitions through a spike. The overall appearance of the osteoderm in X-ray μ-CT and the gradient between mineralization in the *CT* and the *BT* resembles what has previously been reported for the sister taxon *Heloderma suspectum* [18,19,37]. However, in the present case, the *TZ* is more clearly defined by its gradual change in the degree of mineralization (Fig. 1).

One of the osteoderms studied displayed an area of apparent damage that presented high zinc contribution in the XRF, consistent with these late-developing structures being subject to later remodeling [53]. Remodeling is a characteristic of bone in general, and histological evidence of remodeling with osteoderms has been reported [54]. Regeneration has also been reported for osteoderms in other regeneration-competent osteoderm-bearing lizard species [37,55,56]. The osteoderm remodeling may extend to the *CT,* even if further studies are needed to confirm this. Such remodeling would be in stark contrast with the inability of enamel to undergo remodeling.

In terms of mineral composition, zinc was associated with areas of damage and potential repair, as well as at the basal border of the osteoderm, which may represent an area of continued mineralization. Zinc has been found in growth areas, indicating mineralization sites in multiple species. It has been located in the extracellular matrix ahead of and at the mineralization front [40] as a co-factor of multiple metalloproteases [42,43]. Zinc and strontium were localized separately from each other within the osteoderm, with strontium overrepresented within the *CT* and in bands in the Sharpey's fibers in the *BT* of the ventral osteoderm. The contribution of strontium to the mechanical properties of bone is debated and not fully understood.

Synthetic hydroxyapatite doped with Sr ions substituting the Ca atoms in the lattice has been shown to have a higher strength in compressive tests, which varies with the concentration [57]. For biological apatite, *in vitro* studies showed enhanced mechanical performance for Sr-rich hydroxyapatite; however, they also showed that Sr also contributes greatly to the biological compatibility and osteogenic and osteoconductive properties, promoting the formation and growth of new mineralized tissue [58], which will also enhance the mechanical performance of the tissue. This effect has also been observed in vivo in animal models [59] and human studies [60]. While Sr appears in the most mechanically extreme of the tissue subcategories, being highest in the *CT*, separating its effects from the generally higher mineralization level is not possible in this study.

As regards the banding of strontium in the ventral/deep portion of the osteoderm, strontium levels within bio-mineralization can vary with exposure to sources (teeth) [61], but also within mineralized tissue under relatively constant exposure, where its regulation is an area of current study [62,63]. Here, it may vary with collagen presence in the Sharpey fibers *BT*, but a higher resolution would be required to resolve the co-localization of strontium, mechanical properties, and collagen percentage.

The *CT* is primarily made of biomineral consisting of hydroxyapatite nanocrystals and has only minimal, if any, collagen content (**Supporting Figure S11**). The tissue is more highly mineralized than the *BT*, enriched in Sr, and composed of very large and elongated crystals (up to an order of magnitude larger than the crystals found in the *BT*) in an apparent isotropic distribution from the X-ray diffraction results. In contrast, *BT* is less mineralized, with a lower content of Sr and with oriented elongated hydroxyapatite crystals similar in size to the ones found in many other mineralized tissues like in mammals [45]. Scanning electron microscopy confirmed the XRD results, where *BT* presented oriented mineralized collagen fibrils (**Supporting Figure S12b-e** and **S12k-n**), as typically observed in bone [64], while *CT* had mineral clusters with isotropic shape and no evident preferential orientation in the tissue (Supporting **Figure S12f-i** and **S12o-r**).

4.2. Heloderma horridum has the stiffest reported capping tissue

H. horridum CT presents very high stiffness (i.e., elastic modulus) and hardness, up to 5 times higher than that of the *BT*. Importantly, while the mechanical properties of the *BT* agree with previously reported values in lizards [18], the elastic modulus and hardness of *H. horridum CT* are greater than those of other lizard species [18,19,38] and are the highest *CT* stiffness found across different lizard species to date. The values are higher than those reported using nanoindentation for fresh frozen enamel in *H. suspectum* (22.4–39.9 GPa [19]), and overlap with those of dental enamel for the varanid *Varanus niloticus* (55.3–82.9 GPa [19]), tuatara *Sphenodon punctatus* (30 ± 9 to 42 ± 6 GPa) [65], and fresh and fixed enamel from *Alligator mississippiensis* (59–68 GPa) [66], and within the wide range of mammalian enamel values (~80–100 GPa [24,50]). The process of fixation and dehydration in ethanol storage has not been reported to increase enamel hardness or Young's modulus, at least in crocodilian enamel. However, dehydration from storage in ethanol might have an effect. Given the high degree of mineralization of the *CT*, this must be considered when interpreting the raw data from this investigation. Notwithstanding, the higher value for *CT* in the current paper is observed at the most superficial part of the *CT,* which may not have been captured within previous samples [18,19]. Surprisingly, the values of Young's modulus and hardness in *CT* are almost comparable to those found on iron-coated teeth from multiple reptile species, such as *Varanus komodoensis* [44], despite no localized iron being found on the capping tissue in the XRF experiments.

The layering of a highly mineralized layer over a bony, lower-hardness material is also seen in the parrot fish beak, with enameloid being deposited on top of the bone plate [67], or in another manifestation of the reduced dermal skeleton: fish scales, specifically those characterized by a superficial ganoine layer [21]. The *CT*'s Young's modulus is comparable to or higher than the ganoine layer of some fish scales [20,22,68] (e.g., ~62 GPa for *Polypterus senegalus*, and ~69 GPa for alligator gar *Atractosteus spatula*), with slightly lower hardness [21] than the record-setting parrot fish beak enameloid [67].

4.3. Capping tissue has negligible texture in stark contrast to enamel

The most surprising finding of this work is the combination of very large, elongated nanocrystals with almost no texture for a material exhibiting extremely high stiffness. This is highly unusual within a biological context, and we know of no other apatite-based system featuring such extremes. It contrasts dramatically with a more recognized, highly stiff biomineralized tissue - enamel - where the texture of its large and highly oriented hydroxyapatite crystals [23,50,51,69,70] has been correlated with its high hardness [26]. Instead, *CT* in the Mexican beaded lizard shows a different pathway to achieve high stiffness with biomineral hydroxyapatite crystals: a near-isotropic micro and nanostructure of large elongated crystalline particles. *BT*, including that of the ventral portion of the osteoderm studied here, displays lower stiffness in combination with smaller elongated crystals. The lack of orientation of the *CT* crystals raises questions about their growth regulation within the biological tissue, as well as speculation about the functional properties of such isotropic crystals in their resistance to forces applied from different directions to the osteoderm within the skin.

Although no knowledge on the growth of such structure is available at present, beyond its development after that of the underlying osteoderm [7], we hypothesize that the nanostructure anisotropy in the different tissue types is guided by the presence or absence of ordered collagen fibrils or other ordering scaffolds during the osteoderm development and mineralization process. Collagen fibrils act as templates for the mineral crystals' growth. Oriented needle or plate-like particles are created parallel to collagen in the space available [71]. In its absence,

biomineral crystals nucleate and grow freely in any available direction, finding no boundaries in specific directions other than the neighboring particle, and therefore, forming a nearly isotropic mineralized material at the special length scale probed (~10 μm) as seen in the *CT*.

Functionally, the *Heloderma* osteoderms are bead-like (rounded) and separated within the skin; therefore, conspecific tooth forces may be expected to interact with the osteoderm from various directions. Female-female conspecific aggression is noted within the species, with roles in territoriality, courtship tactics, and nest and offspring guarding [72] and male-male aggression has also been reported [73]. The species exhibits anterior bite forces of 35.7 to 94.3 N, and standardized posterior bite force at the most posterior teeth ranged from 55.0 to 145.1 N, where the females are reportedly at the lower end of this range. Therefore, we would expect from the nanoindentation data that the osteoderm with its intriguing capping layer would provide some protection from this bite. When there is a limited availability of building blocks, smart structuring is the key to achieving high performance. Abrupt interfaces between materials with different mechanical properties are subject to localized stress gradients. While this can be beneficial in some cases, such as in the crack deflection mechanisms exhibited by mollusk shells [74,75], it can lead to premature crack formation and catastrophic failure. Graded interfaces in natural materials have been proven to act as energy dissipators and improve the toughness and resistance of the materials [3, 76], such as in the marine worm (annelid) jaws [77–80], the mantis shrimp club [52], in dermal armor in vertebrates [1,17,68], and the tooth enamel-dentine junction [81]. The gradually changing mechanical properties from the *CT* over the *TZ* to the *BT* would help diffuse the applied load [3] and improve the overall performance of the osteoderm in terms of protection against contact damage. In terms of biomimetics, this layer may be of interest given its material characteristics and crystalline microstructure [19,21].

5. Conclusions

We investigated the unique structural and mechanical properties of osteoderms of the Mexican beaded lizard (*Heloderma horridum*) with a particular focus on the outer, superficial, capping tissue. The capping tissue exhibits remarkably high stiffness and hardness, up to five times that of the underlying bone tissue, making it the stiffest capping tissue reported among lizards to date. The capping tissue structure is composed of large, elongated hydroxyapatite nanocrystals arranged near-isotopically, lacking the directional texture typical of other biomineralized tissues such as bone or enamel. Additionally, the capping tissue is low in collagen but enriched in strontium, which also appears in bands within the bone tissue. Possible evidence of remodeling, including zinc-rich areas linked to damage repair, suggests that osteoderms may undergo remodeling and/or repair in response to wear or injury over time.

The bone and capping tissue meet at a graded interphase (transition zone) that is likely to aid in diffusing mechanical loads, potentially protecting the osteoderm under high-pressure conditions. Functionally, this highly mineralized, non-oriented capping tissue layer covering the dorsal superficial surface of the osteoderm may provide resilience against vertical compressive forces at different angles, potentially protecting the lizard from aggressive encounters such as the documented intraspecific aggression [72,73].

This study reveals an unusual structural pathway to achieve extreme hardness and stiffness in biological tissue through a nearly isotropic large biomineral crystal arrangement. This contrasts with both bone and enamel, which rely on highly oriented crystals, suggesting a new potential avenue for designing resilient synthetic materials by mimicking the Mexican beaded lizard capping tissue's microstructural arrangement.

Data and materials availability

All data are available in the main text, the supplementary materials, and the following data repository: 10.5281/zenodo.13136002.

CRediT authorship contribution statement

Adrian Rodriguez-Palomo: Writing – review & editing, Writing – original draft, Investigation, Formal analysis. **Malene Siri Berg Jacobsen:** Writing – review & editing, Investigation. **Thorbjørn Erik Køppen Christensen:** Writing – review & editing, Investigation. **Mads Ry Vogel Jørgensen:** Writing – review & editing, Investigation. **Innokenty Kantor:** Writing – review & editing, Investigation. **Gabriella Willan:** Investigation. **Anthony Herrel:** Writing – review & editing, Resources. **Arsalan Marghoub:** Writing – review & editing. **Mehran Moazen:** Writing – review & editing, Funding acquisition. **Susan Evans:** Writing – review & editing, Funding acquisition. **Matthew Vickaryous:** Writing – review & editing, Funding acquisition. **Catherine J.A. Williams:** Writing – review & editing, Writing – original draft, Investigation, Conceptualization. **Henrik Birkedal:** Writing – review & editing, Writing – original draft, Investigation, Formal analysis, Conceptualization.

Declaration of competing interest

The authors declare that they have no known competing financial interests or personal relationships that could have appeared to influence the work reported in this paper.

Acknowledgments

We acknowledge the MAX IV Laboratory for time on Beamline DanMAX under Proposals 20221426 and 20230245. Research conducted at MAX IV is supported by the Swedish Research Council under contract 2018-07152, the Swedish Governmental Agency for Innovation Systems under contract 2018-04969, and Formas under contract 2019-02496. DanMAX is funded by the NUFI grant no. 4059-00009B The XRF detector was made available by Aarhus University through grant CF18-0802 from the Carlsberg Foundation. We thank the Danish Agency for Science, Technology, and Innovation for funding the instrument center DanScatt. The use of the Novo Nordisk Foundation research infrastructure AXIA (grant NNF19OC0055801) is gratefully acknowledged. The Carlsberg Foundation is acknowledged for funding the Tescan Clara SEM used in this work. Support from Nordforsk (grant number 105053) is gratefully acknowledged. Samples were made available via the HSFP-funded project Human Frontier Science Program (RGP0039/2019).

Supplementary materials

Supplementary material associated with this article can be found, in the online version, at doi:10.1016/j.actbio.2025.08.025.

References

[1] W. Yang, I.H. Chen, B. Gludovatz, E.A. Zimmermann, R.O. Ritchie, M.A. Meyers, Natural flexible dermal armor, Adv. Mater. 25 (1) (2013) 31–48.
[2] P. Fratzl, O. Kolednik, F.D. Fischer, M.N. Dean, The mechanics of tessellations - bioinspired strategies for fracture resistance, Chem. Soc. Rev. 45 (2) (2016) 252–267.
[3] Z. Liu, M.A. Meyers, Z. Zhang, R.O. Ritchie, Functional gradients and heterogeneities in biological materials: design principles, functions, and bioinspired applications, Prog. Mater. Sci. 88 (2017) 467–498.
[4] C. Liang, A. Marghoub, L. Kever, S. Bertazzo, A. Abzhanov, M. Vickaryous, A. Herrel, S.E. Evans, M. Moazen, Lizard osteoderms – Morphological characterisation, biomimetic design and manufacturing based on three species, Bioinspir. Biomim. 16 (6) (2021) 066011.
[5] V. de Buffrénil, Y. Dauphin, J.-C. Rage, J.-Y. Sire, An enamel-like tissue, osteodermine, on the osteoderms of a fossil anguid (Glyptosaurinae) lizard, C. R. Palevol 10 (5) (2011) 427–437.

[6] M. Maden, T. Polvadore, A. Polanco, W.B. Barbazuk, E. Stanley, Osteoderms in a mammal the spiny mouse Acomys and the independent evolution of dermal armor, iScience 26 (6) (2023) 106779.
[7] C. Williams, A. Kirby, A. Marghoub, L. Kéver, S. Ostashevskaya-Gohstand, S. Bertazzo, M. Moazen, A. Abzhanov, A. Herrel, S.E. Evans, M. Vickaryous, A review of the osteoderms of lizards (Reptilia: squamata), Biol. Rev. 97 (1) (2022) 1–19.
[8] P. Frýdlová, V. Janovská, J. Mrzílková, M. Halašková, M. Riegerová, J. Dudák, V. Tymlová, J. Žemlička, P. Zach, D. Frynta, The first description of dermal armour in snakes, Sci. Rep. 13 (1) (2023) 6405.
[9] M.K. Vickaryous, J.-Y. Sire, The integumentary skeleton of tetrapods: origin, evolution, and development, J. Anat. 214 (4) (2009) 441–464.
[10] C. Broeckhoven, Y. El Adak, C. Hui, R. Van Damme, T. Stankowich, On dangerous ground: the evolution of body armour in cordyline lizards, Proc. R. Soc. B: Biol. Sci. 285 (1880) (2018) 20180513.
[11] A. du Plessis, C. Broeckhoven, I. Yadroitsev, I. Yadroitsava, S.G. le Roux, Analyzing nature's protective design: the glyptodont body armor, J. Mech. Behav. Biomed. Mater. 82 (2018) 218–223.
[12] C. Broeckhoven, P.L.l.F.N. Mouton, C. Hui, Proximate causes of variation in dermal armour: insights from armadillo lizards, Oikos 127 (10) (2018) 1449–1458.
[13] C. Broeckhoven, C. de Kock, P.L.F.N. Mouton, Sexual dimorphism in osteoderm expression and the role of male intrasexual aggression, Biol. J. Linn. Soc. 122 (2) (2017) 329–339.
[14] L.L. Inacio Veenstra, C. Broeckhoven, Revisiting the thermoregulation hypothesis of osteoderms: a study of the crocodilian Paleosuchus palpebrosus (Crocodilia: alligatoridae), Biol. J. Linn. Soc. 135 (4) (2022) 679–691.
[15] C. Broeckhoven, A. du Plessis, Osteoderms as calcium reservoirs: insights from the lizard Ouroborus cataphractus, J. Anat. 241 (3) (2022) 635–640.
[16] A. Marghoub, L. Kéver, C.J.A. Williams, A. Abzhanov, M. Vickaryous, A. Herrel, S. E. Evans, M. Moazen, The role of cranial osteoderms on the mechanics of the skull in scincid lizards, Anat. Rec. 306 (10) (2023) 2415–2424.
[17] L. Kéver, D. Olivier, A. Marghoub, S.E. Evans, M.K. Vickaryous, M. Moazen, A. Herrel, Biomechanical behaviour of lizard osteoderms and skin under external loading, J. Exp. Biol. 225 (20) (2022).
[18] F. Iacoviello, A.C. Kirby, Y. Javanmardi, E. Moeendarbary, M. Shabanli, E. Tsolaki, A.C. Sharp, M.J. Hayes, K. Keevend, J.-H. Li, D.J.L. Brett, P.R. Shearing, A. Olivo, I. K. Herrmann, S.E. Evans, M. Moazen, S. Bertazzo, The multiscale hierarchical structure of Heloderma suspectum osteoderms and their mechanical properties, Acta Biomater. 107 (2020) 194–203.
[19] A. Marghoub, C.J.A. Williams, J.V. Leite, A.C. Kirby, L. Kéver, L.B. Porro, P. M. Barrett, S. Bertazzo, A. Abzhanov, M. Vickaryous, A. Herrel, S.E. Evans, M. Moazen, Unravelling the structural variation of lizard osteoderms, Acta Biomater. 146 (2022) 306–316.
[20] P.G. Allison, M.Q. Chandler, R.I. Rodriguez, B.A. Williams, R.D. Moser, C.A. Weiss, A.R. Poda, B.J. Lafferty, A.J. Kennedy, J.M. Seiter, W.D. Hodo, R.F. Cook, Mechanical properties and structure of the biological multilayered material system, Atractosteus spatula scales, Acta Biomater. 9 (2) (2013) 5289–5296.
[21] P. Rawat, D. Zhu, M.Z. Rahman, F. Barthelat, Structural and mechanical properties of fish scales for the bio-inspired design of flexible body armors: a review, Acta Biomater. 121 (2021) 41–67.
[22] B.J.F. Bruet, J. Song, M.C. Boyce, C. Ortiz, Materials design principles of ancient fish armour, Nat. Mater. 7 (9) (2008) 748–756.
[23] J. Wilmers, S. Bargmann, Nature's design solutions in dental enamel: uniting high strength and extreme damage resistance, Acta Biomater. 107 (2020) 1–24.
[24] L.H. He, M.V. Swain, Understanding the mechanical behaviour of human enamel from its structural and compositional characteristics, J. Mech. Behav. Biomed. Mater. 1 (1) (2008) 18–29.
[25] S. Bentov, P. Zaslansky, A. Al-Sawalmih, A. Masic, P. Fratzl, A. Sagi, A. Berman, B. Aichmayer, Enamel-like apatite crown covering amorphous mineral in a crayfish mandible, Nat. Commun. 3 (1) (2012) 839.
[26] C.A. Stifler, J.E. Jakes, J.D. North, D.R. Green, J.C. Weaver, P.U.P.A. Gilbert, Crystal misorientation correlates with hardness in tooth enamels, Acta Biomater. 120 (2021) 124–134.
[27] S. Habelitz, S.J. Marshall, G.W. Marshall, M. Balooch, Mechanical properties of human dental enamel on the nanometre scale, Arch. Oral Biol. 46 (2) (2001) 173–183.
[28] R. Saulnier Masson, K. Daoues, J. Measey, A. Herrel, The evolution of bite force and head morphology in scincid lizards: diet and habitat use as possible drivers, Biol. J. Linn. Soc. 140 (1) (2023) 58–73.
[29] D. Gursoy, F. De Carlo, X. Xiao, C. Jacobsen, TomoPy: a framework for the analysis of synchrotron tomographic data, J. Synchrotron. Radiat. 21 (5) (2014) 1188–1193.
[30] B. Henrich, A. Bergamaschi, C. Broennimann, R. Dinapoli, E.F. Eikenberry, I. Johnson, M. Kobas, P. Kraft, A. Mozzanica, B. Schmitt, PILATUS: a single photon counting pixel detector for X-ray applications, Nucl. Instrum. Methods Phys. Res. A: Accel. Spectrom. Detect. Assoc. Equip. 607 (1) (2009) 247–249.
[31] A.B. Jensen, T.E.K. Christensen, C. Weninger, H. Birkedal, Very large-scale diffraction investigations enabled by a matrix-multiplication facilitated radial and azimuthal integration algorithm: *matFRAIA*, J. Synchrotron. Radiat. 29 (6) (2022) 1420–1428.
[32] S. Frolich, H. Birkedal, MultiRef: software platform for Rietveld refinement of multiple powder diffractograms from in situ, scanning or diffraction tomography experiments, J. Appl. Crystallogr. 48 (6) (2015) 2019–2025.
[33] A.C. Larson, R.B. Dreele, Generalized structure Analysis System (GSAS), Alamos Natl. Lab. Rep. LAUR (2000) 86–789.
[34] V.A. Solé, E. Papillon, M. Cotte, P. Walter, J. Susini, A multiplatform code for the analysis of energy-dispersive X-ray fluorescence spectra, Spectrochim. Acta B: At. Spectrosc. 62 (1) (2007) 63–68.
[35] J.Q.I. Chua, T.E.K. Christensen, J. Palle, N.K. Wittig, T.A. Grünewald, J. Garrevoet, K.M. Spiers, H. Castillo-Michel, A. Schramm, W.L. Chien, R.M. Sobota, H. Birkedal, A. Miserez, Biomineralization of mantis shrimp dactyl club following molting: apatite formation and brominated organic components, Acta Biomater. 170 (2023) 479–495.
[36] W.C. Oliver, G.M. Pharr, An improved technique for determining hardness and elastic modulus using load and displacement sensing indentation experiments, J. Mater. Res. 7 (6) (1992) 1564–1583.
[37] A. Kirby, M. Vickaryous, A. Boyde, A. Olivo, M. Moazen, S. Bertazzo, S. Evans, A comparative histological study of the osteoderms in the lizards Heloderma suspectum (Squamata: helodermatidae) and Varanus komodoensis (Squamata: varanidae), J. Anat. 236 (6) (2020) 1035–1043.
[38] A. Maliuk, A. Marghoub, C.J.A. Williams, E. Stanley, L. Kéver, M. Vickaryous, A. Herrel, S.E. Evans, M. Moazen, Comparative analysis of osteoderms across the lizard body, Anat. Rec. (2024).
[39] T.E.K. Christensen, M. Berglund Davidsen, S. Van Malderen, J. Garrevoet, V. Offermanns, O.Z. Andersen, M. Foss, H. Birkedal, Local release of strontium from sputter-deposited coatings at implants increases the strontium-to-calcium ratio in peri-implant bone, ACS Biomater. Sci. Eng. 8 (2) (2022) 620–625.
[40] I. Silva Barreto, S. Le Cann, S. Ahmed, V. Sotiriou, M.J. Turunen, U. Johansson, A. Rodriguez-Fernandez, T.A. Grünewald, M. Liebi, N.C. Nowlan, H. Isaksson, Multiscale characterization of embryonic long bone mineralization in mice, Adv. Sci. 7 (21) (2020) 2002524.
[41] H. Dejea, D.B. Raina, I. Silva Barreto, K. Sharma, Y. Liu, D. Ferreira Sanchez, U. Johansson, H. Isaksson, Multi-scale characterization of the spatio-temporal interplay between elemental composition, mineral deposition and remodelling in bone fracture healing, Acta Biomater. 167 (2023) 135–146.
[42] T.M. Litchfield, Y. Ishikawa, L.N.Y. Wu, R.E. Wuthier, G.R. Sauer, Effect of metal ions on calcifying growth plate cartilage chondrocytes, Calcif. Tissue Int. 62 (4) (1998) 341–349.
[43] B.R. Genge, G.R. Sauer, L.N. Wu, F.M. McLean, R.E. Wuthier, Correlation between loss of alkaline phosphatase activity and accumulation of calcium during matrix vesicle-mediated mineralization, J. Biol. Chem. 263 (34) (1988) 18513–18519.
[44] A.R.H. LeBlanc, A.P. Morrell, S. Sirovica, M. Al-Jawad, D. Labonte, D.C. D'Amore, C. Clemente, S. Wang, F. Giuliani, C.M. McGilvery, M. Pittman, T.G. Kaye, C. Stevenson, J. Capon, B. Tapley, S. Spiro, O. Addison, Iron-coated Komodo dragon teeth and the complex dental enamel of carnivorous reptiles, Nat. Ecol. Evol. (2024).
[45] A. Rodriguez-Palomo, M. Østergaard, H. Birkedal, Bone hierarchical structure: heterogeneity and uniformity, Adv. Funct. Mater. (2023) 2307026.
[46] A. Rodriguez-Palomo, M. Østergaard, H. Birkedal, Bone hierarchical structure: heterogeneity and uniformity, Adv. Funct. Mater. 34 (2023) 2307026.
[47] N.K. Wittig, J. Palle, M. Østergaard, S. Frølich, M.E. Birkbak, K. Spiers, J. Garrevoet, H. Birkedal, Bone biomineral properties vary across Human osteonal Bone, ACS. Nano 13 (2019) 12949–12956.
[48] Z.Y. Li, W.M. Lam, C. Yang, B. Xu, G.X. Ni, S.A. Abbah, K.M.C. Cheung, K.D.K. Luk, W.W. Lu, Chemical composition, crystal size and lattice structural changes after incorporation of strontium into biomimetic apatite, Biomaterials 28 (7) (2007) 1452–1460.
[49] S.M. Londoño-Restrepo, R. Jeronimo-Cruz, B.M. Millán-Malo, E.M. Rivera-Muñoz, M.E. Rodriguez-García, Effect of the nano crystal size on the X-ray diffraction patterns of biogenic hydroxyapatite from Human, bovine, and porcine bones, Sci. Rep. 9 (1) (2019) 5915.
[50] P.W. Lucas, S.M. Philip, D. Al-Qeoud, N. Al-Draihim, S. Saji, A. van Casteren, Structure and scale of the mechanics of mammalian dental enamel viewed from an evolutionary perspective, Evol. Dev. 18 (1) (2016) 54–61.
[51] E. Beniash, C.A. Stifler, C.-Y. Sun, G.S. Jung, Z. Qin, M.J. Buehler, P.U.P.A. Gilbert, The hidden structure of human enamel, Nat. Commun. 10 (1) (2019) 4383.
[52] J.C. Weaver, G.W. Milliron, A. Miserez, K. Evans-Lutterodt, S. Herrera, I. Gallana, W.J. Mershon, B. Swanson, P. Zavattieri, E. DiMasi, D. Kisailus, The Stomatopod Dactyl Club: a formidable damage-tolerant biological hammer, Science 336 (6086) (2012) 1275–1280.
[53] M.K. Vickaryous, G. Meldrum, A.P. Russell, Armored geckos: a histological investigation of osteoderm development in Tarentola (Phyllodactylidae) and Gekko (Gekkonidae) with comments on their regeneration and inferred function, J. Morphol 276 (11) (2015) 1345–1357.
[54] G. Willan, Histological heterogeneity: Tissue-level diversity of Lizard Osteoderms, University of Guelph, Guelph, Ontario, Canada, 2024.
[55] Y. Pochat-Cottilloux, J.E. Martin, R. Amiot, J. Cubo, V. de Buffrénil, A survey of osteoderm histology and ornamentation among crocodylomorpha: a new proxy to infer lifestyle? J. Morphol. 284 (1) (2023) e21542.
[56] G.O. Cherepanov, D.A. Gordeev, D.A. Melnikov, N.B. Ananjeva, Osteoderm development during the regeneration process in Eurylepis taeniolata Blyth, 1854 (Scincidae, Sauria, Squamata), J. Dev. Biol. (2023).
[57] M. Schumacher, A. Henß, M. Rohnke, M. Gelinsky, A novel and easy-to-prepare strontium(II) modified calcium phosphate bone cement with enhanced mechanical properties, Acta Biomater. 9 (7) (2013) 7536–7544.
[58] M. Cattani-Lorente, R. Rizzoli, P. Ammann, In vitro bone exposure to strontium improves bone material level properties, Acta Biomater. 9 (6) (2013) 7005–7013.
[59] H. Aoki, S. Okayama, M. Akao, Effect of strontium content on the mechanical properties of bone and sintered hydroxyapatite, in: W. Bonfield, G.W. Hastings, K. E. Tanner (Eds.), Bioceramics, Butterworth-Heinemann, 1991, pp. 87–90.

[60] C. Riedel, E.A. Zimmermann, J. Zustin, M. Niecke, M. Amling, M. Grynpas, B. Busse, The incorporation of fluoride and strontium in hydroxyapatite affects the composition, structure, and mechanical properties of human cortical bone, J. Biomed. Mater. Res. A 105 (2) (2017) 433–442.
[61] L.T. Humphrey, M.C. Dean, T.E. Jeffries, An evaluation of changes in strontium/calcium ratios across the neonatal line in human deciduous teeth (Eds., in: S. E. Bailey, J.-J. Hublin (Eds.), Dental Perspectives on Human Evolution: State of the Art Research in Dental Paleoanthropology, Springer, Netherlands, Dordrecht, 2007, pp. 303–319.
[62] S. Chen, R. Zhao, Z. Xing, T. Shang, X. Yang, X. Zhu, X. Zhang, Strontium combined with bioceramics for osteoporotic bone repair: oral intake or as a dopant? Appl. Mater. Today 22 (2021) 100927.
[63] D. Marx, A. Rahimnejad Yazdi, M. Papini, M. Towler, A review of the latest insights into the mechanism of action of strontium in bone, Bone Rep. 12 (2020) 100273.
[64] D.J. Buss, R. Kröger, M.D. McKee, N. Reznikov, Hierarchical organization of bone in three dimensions: a twist of twists, J. Struct. Biol.: X 6 (2022) 100057.
[65] E.D. Yilmaz, S. Bechtle, H. Özcoban, J.A. Kieser, M.V. Swain, G.A. Schneider, Micromechanical characterization of prismless enamel in the tuatara, Sphenodon punctatus, J. Mech. Behav. Biomed. Mater. 39 (2014) 210–217.
[66] J.E. Creech, Phylogenetic Character Analysis of Crocodylian Enamel Microstructure and Its Relevance to Biomechanical Performance, Department of Biological Science, Florida State University, 2004.
[67] M.A. Marcus, S. Amini, C.A. Stifler, C.-Y. Sun, N. Tamura, H.A. Bechtel, D. Y. Parkinson, H.S. Barnard, X.X.X. Zhang, J.Q.I. Chua, A. Miserez, P.U.P.A. Gilbert, Parrotfish teeth: stiff biominerals whose microstructure makes them tough and abrasion-resistant to bite stony corals, ACS Nano 11 (12) (2017) 11856–11865.
[68] W. Yang, B. Gludovatz, E.A. Zimmermann, H.A. Bale, R.O. Ritchie, M.A. Meyers, Structure and fracture resistance of alligator gar (Atractosteus spatula) armored fish scales, Acta Biomater. 9 (4) (2013) 5876–5889.
[69] M. Al-Jawad, A. Steuwer, S.H. Kilcoyne, R.C. Shore, R. Cywinski, D.J. Wood, 2D mapping of texture and lattice parameters of dental enamel, Biomaterials 28 (18) (2007) 2908–2914.
[70] L.M. Simmons, M. Al-Jawad, S.H. Kilcoyne, D.J. Wood, Distribution of enamel crystallite orientation through an entire tooth crown studied using synchrotron X-ray diffraction, Eur. J. Oral Sci. 119 (s1) (2011) 19–24.
[71] N. Reznikov, M. Bilton, L. Lari, M.M. Stevens, R. Kröger, Fractal-like hierarchical organization of bone begins at the nanoscale, Science 360 (6388) (2018) eaao2189.
[72] G.W. Schuett, K.H. Peterson, A.R. Powell, J.D. Taylor, J.R. Alexander, A.K. Lappin, Female–female aggression in the Gila monster (*Heloderma suspectum*), R. Soc. Open Sci. 10 (5) (2023) 221466.
[73] D.D. Beck, A. Ramírez-Bautista, Combat behavior of the beaded lizard, heloderma h. horridum, in Jalisco, México, J. Herpetol. 25 (4) (1991) 481–484.
[74] J. Sun, B. Bhushan, Hierarchical structure and mechanical properties of nacre: a review, RSC Adv. 2 (20) (2012) 7617–7632.
[75] S. Frølich, J.C. Weaver, M.N. Dean, H. Birkedal, Uncovering nature's design strategies through parametric modeling, multi-material 3D printing, and mechanical testing, Adv. Eng. Mater. 19 (6) (2017) e201600848.
[76] J.H. Waite, H.C. Lichtenegger, G.D. Stucky, P. Hansma, Exploring molecular and mechanical gradients in structural bioscaffolds, Biochemistry 43 (24) (2004) 7653–7662.
[77] H.C. Lichtenegger, T. Schöberl, M.H. Bartl, H. Waite, G.D. Stucky, High abrasion resistance with sparse mineralization: copper biomineral in worm jaws, Science 298 (5592) (2002) 389–392.
[78] H. Birkedal, R.K. Khan, N. Slack, C. Broomell, H.C. Lichtenegger, F. Zok, G. D. Stucky, J.H. Waite, Halogenated veneers: protein cross-linking and halogenation in the jaws of Nereis, a marine polychaete worm, Chembiochem 7 (9) (2006) 1392–1399.
[79] H.C. Lichtenegger, T. Schöberl, J.T. Ruokolainen, J.O. Cross, S.M. Heald, H. Birkedal, J.H. Waite, G.D. Stucky, Zinc and mechanical prowess in the jaws of Nereis, a marine worm, Proc. Natl. Acad. Sci. 100 (16) (2003) 9144–9149.
[80] H.C. Lichtenegger, H. Birkedal, D.M. Casa, J.O. Cross, S.M. Heald, J.H. Waite, G. D. Stucky, Distribution and role of trace transition metals in glycera worm jaws studied with synchrotron microbeam techniques, Chem. Mater. 17 (11) (2005) 2927–2931.
[81] V. Imbeni, J.J. Kruzic, G.W. Marshall, S.J. Marshall, R.O. Ritchie, The dentin–enamel junction and the fracture of human teeth, Nat. Mater. 4 (3) (2005) 229–232.